Applied Energy 212 (2018) 786–795

Contents lists available at ScienceDirect

Applied Energy

journal homepage: www.elsevier.com/locate/apenergy

Co-combustion thermal conversion characteristics of textile dyeing sludge and pomelo peel using TGA and artificial neural networks

Candie Xie[a], Jingyong Liu[a,*], Xiaochun Zhang[a], Wuming Xie[a], Jian Sun[a], Kenlin Chang[a,b], Jiahong Kuo[a], Wenhao Xie[a], Chao Liu[a], Shuiyu Sun[a], Musa Buyukada[c], Fatih Evrendilek[c]

[a] School of Environmental Science and Engineering, Institute of Environmental-Health and Pollution Control, Guangdong University of Technology, Guangzhou 510006, China
[b] Institute of Environmental Engineering, National Sun Yat-Sen University, Kaohsiung 80424, Taiwan
[c] Department of Environmental Engineering, Abant Izzet Baysal University, Bolu 14052, Turkey

HIGHLIGHTS

- Co-combustion of TDS and PP was studied under O_2/N_2 and O_2/CO_2 atmospheres.
- Principal component analysis was used to identify the principal reactions.
- The interaction of blends occurred mainly between 490 and 600 °C.
- Bayesian regularized network had a more reliable and robust prediction.
- The lowest activation energy was obtained under 30% O_2/70% CO_2 atmosphere.

ARTICLE INFO

Keywords:
Oxy-fuel combustion
Textile dyeing sludge
Pomelo peel
Thermogravimetric analysis
Artificial neural networks
Principal component analysis

ABSTRACT

Co-combustion characteristics of textile dyeing sludge (TDS) and pomelo peel (PP) under O_2/N_2 and O_2/CO_2 atmospheres were investigated using a thermogravimetric analysis (TGA) and artificial neural networks. 30% O_2/70% CO_2 and air atmospheres led to a similar co-combustion performance. Increases in O_2 concentration and PP significantly improved the oxy-fuel co-combustion performance of TDS. Principal component analysis was applied to reduce the dimensionality of differential TGA curves and to identify the principal reactions. The interaction between TDS and PP occurred mainly at 490–600 °C, thus improving the process of residue co-combustion. Radial basis function was found to have more reliable and robust predictions of TGA under different O_2/CO_2 atmospheres than did Bayesian regularized network. Regardless of Flynn-Wall-Ozawa (FWO) and Kissinger-Akahira-Sunose (KAS) methods used, the lowest mean value of apparent activation energy (155.4 kJ·mol^{-1} by FWO and 153.2 kJ·mol^{-1} by KAS) was obtained under the 30% O_2/70% CO_2 atmosphere.

1. Introduction

The textile industry constitutes one of the traditional pillar industries of China and has been rapidly growing for the recent decades. In parallel have come the increased discharge amount and rate of highly polluted wastewater and sludge threatening the public and environmental health [1,2]. Currently, textile dyeing industries in China generate wastewater and sludge at annual rates of about 2.1 billion tons (t) and 21 million t, respectively [3]. Textile dyeing sludge (TDS) has a complex composition of dyes, auxiliaries, perishable organics, pathogens, surfactant, heavy metals, and persistent biodegradation products such as polycyclic aromatic hydrocarbons [4]. Its traditional disposals in landfills and soils are not considered socially and environmentally acceptable [5]. Instead, co-combustion of TDS appears to be an alternative and efficient way of disposal owing to reduction of fuel costs, wastes, and risks of environmental pollution, and stabilization of combustion [6–8].

Co-combustion of TDS with biomass has been reported to offset the shortcomings of mono-combustion [9,10]. For example, Cai et al. [11] found that the addition of eucalyptus residues to paper mill sludge improved the mono-combustion characteristics. Zhang et al. [12] reported that adding rice straw to sewage sludge significantly reduced the release of volatiles during their co-pyrolysis process. Peng et al. [7] pointed out that the interaction between microalgae and TDS exerted a

* Corresponding author.
E-mail addresses: www053991@126.com, Liujy@gdut.edu.cn (J. Liu).

https://doi.org/10.1016/j.apenergy.2017.12.084
Received 8 August 2017; Received in revised form 17 November 2017; Accepted 24 December 2017
Available online 04 January 2018
0306-2619/

positive char catalytic effect on the decomposition of TDS residue at 530–800 °C.

With the reduction of fossil fuel reserves, the significance of biofuels has grown as a clean, sustainable and renewable energy source. Co-combustion of biomass accounts for over 97% of bioenergy production globally and in China [13]. In particular, citrus peels as a byproduct in vast amounts are produced after industrial processing of an annual global production of citrus fruits of over 115 million t [14]. For example, pomelo as one of citrus fruits has an annual production of over 2 million t [15], and a large amount of pomelo peels (PP) are dumped into landfills in China. Therefore, PP presents unexplored potential for co-combustion process and energy utilization.

Given the urgent need to reduce CO_2 emissions from fossil fuel combustion, the development of oxy-fuel (O_2/CO_2) co-combustion technology towards carbon capture and storage has been extensively promoted recently [16–18]. Higher CO_2 removal and capture was reported to come from flue gases generated by oxy-fuel co-combustion (~95%) than by the conventional air co-combustion (~15%), which in turn lower costs associated with CO_2 sequestration [19,20]. The replacement of N_2 by CO_2 adversely affects heat transfer rate, gas temperature, and burning stability during the co-combustion process [21]. These negative effects can be mitigated by increased O_2 concentrations during the oxy-fuel co-combustion process [22].

Overall, a better understanding of oxy-fuel combustion calls for experimentally monitoring and modeling of time-series data from a wide range of interacting variables. Machine learning techniques such as artificial neural networks (ANN) have been widely accepted to tackle such complex issues owing to their strong ability of mapping non-linear behaviors [23]. It is possible to estimate oxy-fuel combustion properties based on a minimal set of uniform experimental data. There exist many ANN architectures [24,25] such as Levenberg-Marquardt network (LMN), Bayesian regularized network (BRN) and radial basis function (RBF). LMN was successfully used to predict thermogravimetric analysis (TGA) and differential thermogravimetric (DTG) curves at different heating rates during the co-combustion process [26,27]. However, there have been a few studies adopting BRN and RBF to predict co-combustion properties.

The objectives of the present study were to (1) characterize the co-combustion process of TDS and PP using TGA under the six atmospheres: air (O_2/N_2), 20% O_2/80% CO_2, 30% O_2/70% CO_2, 50% O_2/50% CO_2, 70% O_2/30% CO_2, and O_2, (2) evaluate it using characteristic co-combustion and interaction indices, (3) predict the thermal behaviors of oxy-fuel co-combustion reactions using BRN and RBF, (4) quantify the co-combustion kinetics using the Flynn-Wall-Ozawa (FWO) and Kissinger-Akahira-Sunose (KAS) methods, and (5) perform dimensionality reduction and clustering of DTG data using principal component analysis (PCA). Thus, the co-combustion characteristics of TDS and PP under O_2/N_2 and O_2/CO_2 atmospheres were studied for the first time, as an effective way to improve the mono-combustion performance of TDS. PCA was firstly used to identify the principal reactions during the oxy-fuel co-combustion process. RBF and BRN applied to predict TGA curves during the oxy-fuel co-combustion process constituted another novelty of this study.

2. Methods

2.1. Sample preparation

TDS and PP samples were taken from a textile printing and dyeing plant located in Dongguan and a fruit market of Guangzhou University Mega Center, Guangzhou, China, respectively. The TDS and PP samples were firstly dried in the oven at 105 °C for 24 h to remove moisture. Then, these samples were milled and sieved separately to 200 mesh (74 μm) particle size. TDS blends with 10%, 20%, 30% and 40% (wt%) PP were prepared and coded as TP91, TP82, TP73 and TP64, respectively. The ultimate and proximate analyses were presented in Table 1.

2.2. Thermogravimetric analysis

A TG analyzer (NETZSCH STA 409 PC Luxx, Germany) was used in thermogravimetric experiments. In TG, each sample (10 ± 0.5 mg) were heated from room temperature to 1000 °C using the heating rates of 10, 20 and 30 °C·min^{-1}. The carrier gases were air, O_2/CO_2 and O_2 atmospheres respectively, at a total gas flow rate of 50 mL·min^{-1}. All the experiments were conducted three times in one testing condition for acceptable repeatability, and the relative errors under identical conditions were within ± 2%.

2.3. Combustion parameters

Combustion performance was evaluated using parameters obtained from TGA-DTG curves. The TGA-DTG tangent method was used to determine ignition temperature (T_i) [30]. Burnout temperature (T_f) was defined as the temperature at which 98% conversion is achieved at the end of the reaction [20]. Comprehensive combustion index (*CCI*) was used to evaluate combustion property [31]. A higher *CCI* value means a better combustion property. Combustion stability index (R_w) was used to reflect combustion stability [32]. A higher R_w value indicates better combustion stability.

$$CCI = \frac{R_p \times R_v}{T_i^2 \times T_f} \tag{1}$$

$$R_w = 8.5875 \times 10^7 \times \frac{R_p}{T_i \times T_m} \tag{2}$$

where R_p and R_v are maximum and average mass loss rates, respectively. T_m is the peak temperature.

2.4. Interaction indices (MR-RMS)

Interactions between TDS and PP during the co-combustion were analyzed using theoretical DTG curves (DTG_{theo}) as was presented in Eq. (3) [30]:

$$DTG_{theo} = x_{TDS} \cdot DTG_{TDS} + x_{PP} \cdot DTG_{PP} \tag{3}$$

where x_{TDS} and x_{PP} refer to TDS and PP mass fractions, while DTG_{TDS} and DTG_{PP} represent DTG curves of the pure TDS and PP, respectively.

To evaluate the interactions between each blend, the MR and RMS indices were adopted [33] and defined using Eqs. (4) and (5).

$$MR = \sum_{i=1}^{n} (x_{exp}^i - x_{theo}^i)/n x_{theo}^{mean} \tag{4}$$

$$RMS = \left(\left(\sum_{i=1}^{n} ((x_{exp}^i - x_{theo}^i)/x_{theo}^i)^2 \right) \Big/ n \right)^{1/2} \tag{5}$$

where x_{exp}^i and x_{theo}^i refer to experimental and theoretical values, respectively; and n refer to the sum of experimental points. A positive MR value means a synergetic behavior, while RMS value determines the intensity of the interaction.

2.5. Predictive modeling

Back-propagation (BP) and RBF networks are both the common techniques of feed-forward ANN modeling. The feed-forward ANN architecture for supervised learning applications consists of three layers: input, hidden and output. In the designed networks, mixing ratio, heating rates, combustion atmosphere and temperature were selected as the inputs, while the mass loss percent was selected as the output. To test prediction accuracy and robustness of both ANN models, the TGA data sets were divided into training (95%) and testing (validation) subsets (5%). Due to the small portion of the data, the leave-one-out cross-validation (LOOCV) technique was used in model selection and

Table 1
The ultimate and proximate analyses of TDS and PP on an air-dried basis.

Sample	Ultimate analyses (wt%)					Proximate analyses (wt%)				$Q_{net,d}$[b] ($MJ \cdot kg^{-1}$)
	C	H	O[a]	N	S	M[c]	V[d]	A[e]	FC[f]	
TDS	20.20	6.08	20.00	3.22	2.76	11.70	44.71	36.04	7.55	9.87
PP	42.40	6.31	35.06	0.59	0.01	13.57	68.04	2.06	16.33	16.82

[a] O, calculated by O = 100%–C–H–N–S–M–A [28,29].
[b] $Q_{net,\ d}$, lower heating value on dry basis.
[c] M, moisture.
[d] V, volatile matters.
[e] A, ash.
[f] FC, fixed carbon.

parameter optimization.

2.5.1. RBF

Radial Basis Function is composed of an input layer, a hidden radial basis layer of nodes with Gaussian function, and an output linear layer. In theory, RBF is able to smoothly approximate any nonlinear function if the amounts of nodes in the hidden layer are enough. The newrb function of MATLAB was called to create a three-layer RBF as follows:

$$\text{Net} = \text{newrb (P,T,GOAL,SPREAD,MN,DF)} \tag{6}$$

where P is the input vector; T is the output vector; GOAL is the mean square error; SPREAD is the distribution density of radial basis functions; MN is the maximum number of neurons; DF is the number of neurons added between two iterations.

Training of RBF created by using newrb function is a process by which the iteration was designed by increasing the number of hidden neurons constantly, which continued until the error achieved the target, or the number of neurons reached the upper limit. The training parameters of RBF were presented in Table 2.

2.5.2. BRN

BRN, one of the typical back-propagation (BP) ANNs, is based on Bayesian regularization algorithm that greatly improves the generalization ability by modifying the objective function of ANNs. The mean sum of squares of the network errors (MSE) is the usual choice for the objective function. Therefore, the regularized objective function, the mean square error of regularization (msereg), is given thus [34]:

$$msereg = \alpha(MSE) + \beta(MSW) \tag{7}$$

where:

$$MSE = \frac{1}{N}\sum_{i=1}^{N} e_i^2 = \frac{1}{N}\sum_{i=1}^{N} (y_i - \hat{y}_i)^2 \tag{8}$$

$$MSW = \frac{1}{N}\sum_{i=1}^{N} w_i^2 \tag{9}$$

Table 2
Training parameters selection for RBF and BRN.

Model	Training parameters
RBF	Training function = 'newrb' Spread of the radial basis function = 3.5 Maximum number of neuros = 3800 Maximum epochs = 50 Training goal = 0.006
BRN	Training function = 'trainbr' Number of neurons in hidden layer = 16 Maximum epochs = 500 Maximum validation failures = 50 Learning rate = 0.005 Training goal = 0.0005

while α and β are regularization parameters; y and $\hat{y}$ are the actual and calculated outputs, respectively; N is the total number of parameters in the network; MSW is the sum of squared network weights, and w is the network weight.

The weights and biases in the networks were further optimized by using this objective function that is conductive to overcoming the overfitting problem and improving the generalizing performance of ANNs. Bayesian regularized network was trained using 'trainbr' function in MATLAB 2012a. The training parameters of BRN were presented in Table 2.

2.5.3. Performance indices

To evaluate performance of both ANN models, root mean square error (RMSE), mean absolute error (MAE), and coefficient of determination (R^2) were calculated using Eqs. (10)–(12):

$$RMSE = \sqrt{\frac{1}{N}\left(\sum_{i=1}^{N} (y_i - \hat{y}_i)^2\right)} \tag{10}$$

$$MAE = \frac{1}{N}\left(\sum_{i=1}^{N} |y_i - \hat{y}_i|\right) \tag{11}$$

$$R^2 = 1 - \frac{\sum_{i=1}^{N} (y_i - \hat{y}_i)^2}{\sum_{i=1}^{N} (y_i - \bar{y})^2} \tag{12}$$

where y_i is the actual value from experimental sample, $\hat{y}_i$ is the corresponding predicted value, $\bar{y}$ is the mean of all values from experimental data sets, and N is the number of test data points. Smaller RMSE and MAE values and high R^2 value indicate better model performance.

2.6. Kinetic theory

The kinetics for the overall reaction rate in gas-solid reaction can be generally written as follows:

$$\frac{d\alpha}{dt} = k(P_{O_2}, T) f(\alpha) \tag{13}$$

where k is the apparent combustion reaction rate, which includes the effect of temperature (T) and the effect of the reactive oxygen partial pressure (P_{O_2}), and where α is the conversion degree of solid reactant; $f(\alpha)$ is the reaction model. Assuming that the partial pressure related to the oxygen partial pressure remains constant during the process, the apparent combustion reaction rate will be dependent on the temperature [21,35], thus:

$$\frac{d\alpha}{dt} = \beta\frac{d\alpha}{dT} = k(T) f(\alpha) = A \exp\left(-\frac{E_a}{RT}\right) f(\alpha) \tag{14}$$

where $k(T)$ is the constant of reaction rate; A is the apparent pre-exponential factor (min^{-1}); E_a is activation energy ($kJ \cdot mol^{-1}$); R is the

gas constant (8.314 J·mol^{-1}·K^{-1}); T is the absolute temperature (K); t is the reaction time (min); and β is the heating rate (°C·min^{-1}).

α was defined as follow:

$$\alpha = \frac{m_0 - m_t}{m_0 - m_f} \tag{15}$$

where m_0, m_t and m_f are initial weight, weight at time t and final weight, respectively.

The integrated form of Eq. (14) can be expressed as:

$$g(\alpha) = \int_0^\alpha \frac{d\alpha}{f(\alpha)} = \frac{A}{\beta}\int_0^T \exp\left(-\frac{E_a}{RT}\right)dT = \frac{AE_a}{\beta R}\int_x^\infty \frac{\exp(-x)}{x^2}dx = \frac{AE_a}{\beta R}p(x) \tag{16}$$

where $x = E_a/RT$, and $p(x)$ is the temperature integral without an exact analytical solution.

The FWO and KAS methods were used to estimate the activation energy for non-isothermal thermal experiments. The FWO method is based on the following equation [36]:

$$\log\beta = \log\left(\frac{AE_a}{Rg(\alpha)}\right) - 2.315 - 0.4567\frac{E_a}{RT} \tag{17}$$

where E_a values were estimated from the slope of a plot of log β versus $1/T$ ($-0.4567\ E_a/R$).

The KAS method was derived from the Coats-Redfern approximation of $p(x) = x^{-2}e^{-x}$ as follows [9]:

$$\ln\left(\frac{\beta}{T^2}\right) = \ln\left(\frac{AR}{E_a g(\alpha)}\right) - \frac{E_a}{RT} \tag{18}$$

where E_a values were calculated from plotting $\ln(\beta/T^2)$ versus $1/T$.

2.7. Principal component analysis

Due to the large amount of experimental data from the DTG curves obtained, PCA using a factor analysis function of SPSS 19.0 software was employed to identify the main reactions. In PCA, the DTG data of the samples (TDS, TP91, TP82, TP73, TP64 and PP) were used as the input variables. After the variables were standardized using the descriptive function, the factor extraction and the orthogonal rotation with Kaiser Normalization method was conducted. Our results were presented in the score plots.

3. Result and discussion

3.1. Co-combustion characteristics under six atmospheres

According to previous studies about the interactions during the co-combustion under the air atmosphere, more promoting effects occurred with TP73 which was further used to discuss the effect of the changing co-combustion atmosphere. In the six atmospheres, the TGA and DTG curves obtained for TP73 at 20 °C·min^{-1} were shown in Fig. 1, while the co-combustion characteristic parameters of TP73 were presented in Table 3.

The TGA and DTG curves under the O_2/CO_2 and O_2 atmospheres were similar below 230 °C (Fig. 1), and an exception occurred under the 20% O_2/80% CO_2 atmosphere. All the DTG curves between 150 °C and 230 °C almost superposed with each other which corresponded to the drying and release of light volatiles from the sample. The different atmospheres had no significant effect on this stage of the thermal decomposition of TP73 where temperature rather than atmosphere was the main driving force [37]. In the temperature range of 230–600 °C, the TGA and DTG curves shifted to the lower temperature gradually with the increased O_2 content. The main decomposition process focused on 200–600 °C, taking up at least 81% of the total conversion in either atmosphere. Four weight loss peaks occurred clearly in this stage. For

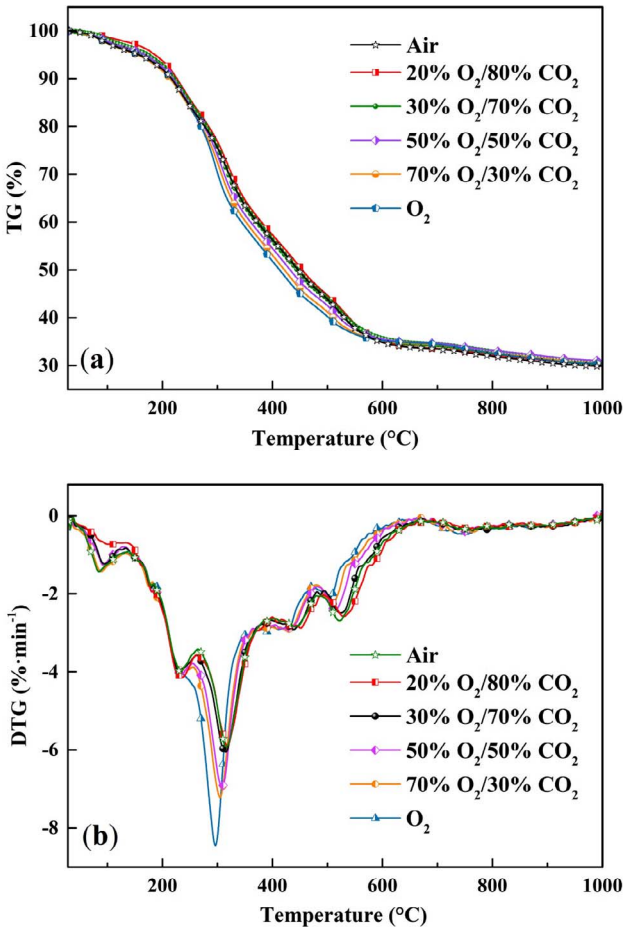

Fig. 1. (a) TGA and (b) DTG curves of TP73 co-combustion at 20 °C·min^{-1} under six atmospheres.

Table 3
Characteristic parameters for TP73 at 20 °C·min^{-1} under six atmospheres.

Atmospheres	T_i[a] (°C)	T_f[b] (°C)	T_m[c] (°C)	R_p[d] (%·min^{-1})	M_f[e] (%)	CCI[f] (10^{-7})	R_w[g] (10^8)
Air	202.5	846.2	315.6	5.92	29.89	2.608	0.0080
20% O_2/80% CO_2	201.9	845.0	317.9	5.88	30.29	2.599	0.0079
30% O_2/70% CO_2	200.8	862.8	315.1	6.05	30.65	2.632	0.0082
50% O_2/50% CO_2	199.5	857.8	308.3	6.92	31.07	3.049	0.0097
70% O_2/30% CO_2	198.3	860.2	304.8	7.21	30.50	3.241	0.0102
O_2	196.8	854.2	296.3	8.45	30.39	3.902	0.0124

[a] T_i, ignition temperature.
[b] T_f, burnout temperature.
[c] T_m, peak temperature.
[d] R_p, maximum mass loss rate.
[e] M_f, residual mass.
[f] CCI, comprehensive combustion index expressed in%^{2}·°C^{-3}·min^{-2}.
[g] R_w, combustion stability index.

example, under the 30% O_2/70% CO_2 atmosphere, the weight loss peaks were centered at 229.4 °C, 315.1 °C and 524.6 °C, while a relatively small one was centered at 438.9 °C. The first three peaks were attributed to the release of volatiles and the decomposition of macromolecule organic matters, while the last one stemmed mainly from char combustion. The weight loss rate reached its maximum at the second peak, which became sharper with the increased O_2 concentration. A higher O_2 concentration increased the mass flux rate of O_2 to the particle surface, thus promoting the fiercer release of the volatiles [38]. This provided extra heat feedback to the particle, enhancing devolatilization and combustion [39]. In contrast, the last weight loss peak

became smaller with the increased O_2 concentration. This result revealed that the other operating conditions such as fuel type were most likely to play more important roles in the last peak value.

Several co-combustion characteristics were determined (Table 2) to validate the effects of O_2 concentration on the co-combustion performance. As expected, as O_2 concentration increased from 20% to 100% under the O_2/CO_2 conditions, ignition (T_i) and peak temperatures (T_m) decreased by 5.1 °C and 21.6 °C, respectively. At the same time, the maximum mass loss rate (R_p) increased from 5.88%·min^{-1} to 8.45%·min^{-1}. Comprehensive combustion index rose by 50.13%, while combustion stability index (R_w) was enhanced by 56.96%. The combustion performance under the O_2/CO_2 atmosphere was significantly improved with the increased O_2 concentration. T_i value barely changed regardless of the O_2/CO_2 conditions which may be attributed to the oxidation of TP73 before ignition in a kinetic controlled region. This conclusion was also supported by the results obtained for coals by Wang et al. [35]. However, the residual mass (M_f) was not correlated with the O_2 concentrations. Similar observations were reported by Huang et al. [31].

The TGA and DTG curve for the co-combustion of TP73 was also presented under air (Fig. 1) relative to the O_2/CO_2 conditions. Weight loss of TP73 in air was similar to that of TP73 in 30% O_2/70% CO_2, in particular, in the temperature range of 200–500 °C. However, when the temperature rose above 600 °C, the beginning of weight loss in air was earlier than in 30% O_2/70% CO_2 corresponding to the appearance orders of the weight loss peak. The higher specific heat and density of CO_2 and lower diffusivity of O_2 in CO_2 than N_2 weakened the transport of O_2 to the particle surface [40,41]. This resulted in the reduced combustion rate under oxy-fuel conditions, as reported elsewhere [35]. As shown in Table 3, the values of T_m, R_p, R_w and *CCI* obtained from these atmospheres were in the following order: 20% O_2/80% CO_2 < air < 30% O_2/70% CO_2 < 50% O_2/50% CO_2 < 70% O_2/30% CO_2 < O_2, as were discussion above. Moreover, the higher O_2 fractions were needed in oxy-fuel co-combustion than in air to achieve better co-combustion performance [42]. The M_f value (30.65%) was higher in 30% O_2/70% CO_2 than air (29.89%) which was consistent with the results obtained for pulverized coal combustion by Li et al. [43]. This case was attributed to the lower flame propagation speed and stability in O_2/CO_2 than air, which led to a higher unburned carbon content [41].

3.2. Co-combustion characteristics under O_2/CO_2 atmosphere

The co-combustion under the 30% O_2/70% CO_2 atmosphere was discussed in this section as it is analogous to the real oxy-fuel co-combustion condition, relative to the 20% O_2/80% CO_2. Fig. 2 showed TGA and DTG curves of the individual fuels and their blends under the 30% O_2/70% CO_2 atmosphere. Table 4 showed the characteristic parameters obtained from the co-combustion under the 30% O_2/70% CO_2 atmosphere.

Principal component analysis was applied to reduce the dimensionality of DTG curves and to identify the principal reactions [44]. The first principal component (PC1) and the second principal component (PC2) were extracted when rotation was converged in three iterations later. PC1 and PC2 accounted for 70.8% and 27.5% of the total variance, respectively, which contributed 98.3% of the sums of squared loadings (meeting the typical threshold of 80%). The score plot (Fig. 2c) showed that the samples belonged to the two separated groups. All the blends and TDS belonged to the same group, thus indicating that TDS had a more complex composition than did PP in affecting the thermal properties. The principal reactions occurred in the combustion process were identified in Fig. 2d, which provided the indication of thermodynamic pattern for PC1 and PC2. The component matrix revealed that TDS was closely related to PC1, and PP was mostly related to PC2. As shown in Fig. 2d, the weight loss peaks of PC1 were indicated to contribute to each stage, whereas PC2 played a major role in the stages 1 and 3. Therefore, the main co-combustion process was divided into the four stages. The stages 1 (200–325 °C) and 2 (325–428 °C) were related to the release of different organic volatiles from PP and TDS. The stage 3 (428–496 °C) corresponded to the combustion of the fixed carbon from PP and difficultly decomposed volatiles from TDS. The stage 4 (496–600 °C) was mainly contributed to by the combustion of the fixed carbon from TDS.

As shown in Fig. 2(a), the curves of the blends fell between those of the pure TDS and PP sequentially, and the weight loss for all mainly occurred between 200 °C and 600 °C. More intense releases of volatiles appeared to occur from the combustion of pure PP than pure TDS, mainly due to larger amounts of hemicellulose, cellulose and other combustible components, higher organic matter content, and lower ash content of PP. Therefore, an earlier weight loss was observed for the TP blends than pure TDS, and their curves gradually shifted from that of TDS to PP. Similar results were also reported in the related literature of co-pyrolysis petrochemical wastewater sludge with lignite [45]. The amount of volatiles release from the blends increased with the increased proportion of PP in the blends from 10% to 40%, leading to the decrease in T_i (204.1–199.3 °C) (Table 4). The impact of the blending with PP on the residual mass was apparent under the 30% O_2/70% CO_2 atmosphere, showing a 12.18% decrease with the increased PP ratio (10–40%).

As can be seen from Fig. 2(b), the DTG curves of the blends had several weight loss peaks and varied depending on the PP blending ratio. With the rising proportion of PP, the characteristic DTG peaks increased. This may be attributed to the decomposition of low-molecular-weight volatiles in PP [46]. For example, R_p value of the blends increased from 4.34%·min^{-1} to 7.12%·min^{-1} with the increased PP (10–40%) (Table 4). At the same time, T_i decreased from 204.1 °C to 199.3 °C, indicating an improved ignition performance and oxy-fuel co-combustion. More significantly, the T_f value decreased by 36 °C, which may result from the fact that the caking process between TDS particles was prevented by the blending of PP [47]. According to Table 4, with the increased PP proportion, T_m decreased from 323.5 °C to 313.3 °C. *CCI* and R_w increased by 1.16 times and 75%, respectively. T_m is considered to be inversely correlated with the reactivity of the fuels [48], which indicates that the reactively of TDS was promoted with the addition of PP. In conclusion, the blending of PP with TDS significantly improved the co-combustion performance under the 30% O_2/70% CO_2 atmosphere.

With the increased PP proportion, the DTG peaks shifted to a lower temperature range, as discussed above. This reflected interactions during the co-combustion under the 30% O_2/70% CO_2 atmosphere. Similar results were reported by Liao and Ma [49]. The experimental and theoretical co-combustion DTG curves were plotted under the 30% O_2/70% CO_2 atmosphere at 20 °C·min^{-1} with the four PP ratios in Fig. 3. As shown in Fig. 3(a)–(d), the theoretical DTG curves matched well with the experimental DTG curves in the temperature ranges of 30–200 °C and 600–1000 °C, while the significant deviations appeared in the temperature range of 200–600 °C. This suggested that interactions existed between the two components during the co-combustion, which was more pronounced with the higher PP proportion.

Fig. 4 showed the interaction indices of RMS and MR in the different stages under the 30% O_2/70% CO_2 atmosphere at 20 °C·min^{-1}. As was shown in Fig. 4(a), the RMS values were greater in the reaction stage 4 (496–600 °C) than in the other stages for all the samples. This case confirmed that the interaction between TDS and PP became more significant at high temperature. As was shown in Fig. 4(b), the MR values were slightly < 0 in the stage 1 for all the samples, indicating that the co-combustion was inhibited slightly in this stage. In particular, the MR values in the stage 3 tended to be < 0, revealing that the inhibition slightly increased in this stage with the increased PP percentage. On the contrary, the MR values in the stage 4 were significantly > 0, indicating that this stage was beneficial during the co-combustion process. This might be attributed to the char formed during the PP combustion, which in turn acted as a catalyst during the decomposition of TDS

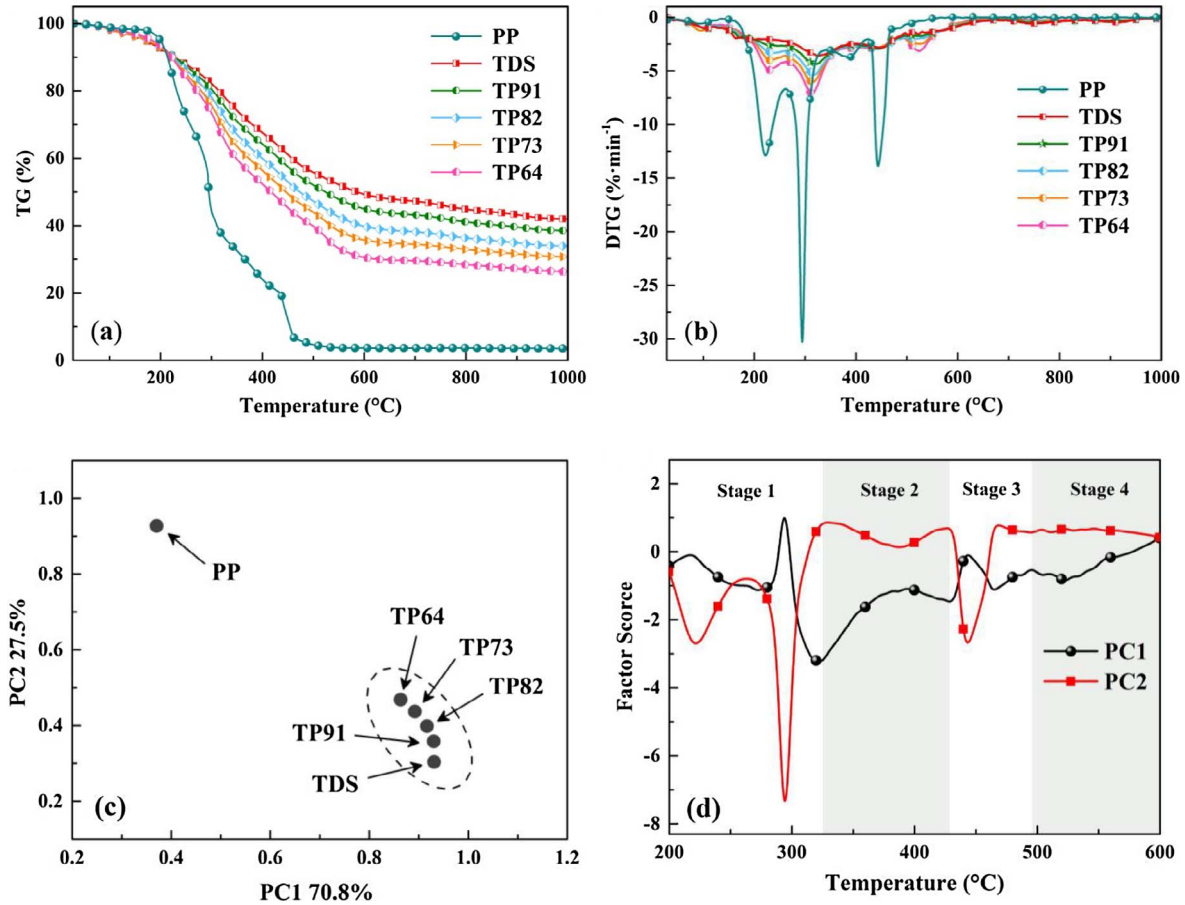

Fig. 2. (a) TGA and (b) DTG curves at 20 °C·min^{-1} under 30% O_2/70% CO_2 atmosphere. (c) Score plot resulting from PCA; and (d) factor scores of PC1 and PC2.

Table 4
Characteristic parameters at 20 °C·min^{-1} under 30% O_2/70% CO_2 atmosphere.

Samples	T_i[a] (°C)	T_f[b] (°C)	T_m[c] (°C)	R_p[d] (%·min^{-1})	M_f[e] (%)	CCI[f] (10^{-7})	R_w[g] (10^{8})
PP	196.0	481.4	294.4	30.28	3.57	36.003	0.0451
TDS	247.2	903.6	325.7	3.63	42.04	0.830	0.0039
TP91	204.1	889.8	323.5	4.34	38.49	1.565	0.0056
TP82	202.2	873.4	318.2	5.34	33.95	2.148	0.0071
TP73	200.8	862.8	315.1	6.05	30.65	2.632	0.0082
TP64	199.3	853.8	313.3	7.12	26.31	3.377	0.0098

[a] T_i, ignition temperature.
[b] T_f, burnout temperature.
[c] T_m, peak temperature.
[d] R_p, maximum mass loss rate.
[e] M_f, residual mass.
[f] CCI, comprehensive combustion index expressed in%^{2}·°C^{-3}·min^{-2}.
[g] R_w, combustion stability index.

residue. The PP combustion in this stage also released more heat to facilitate the endothermic reaction. As a result, the combustion of TDS residue was improved. Similar results were presented in related literature about the co-combustion between microalgae and TDS [7].

3.3. ANN models for co-combustion under O_2/CO_2 atmospheres

In the training process of RBF, the iterations continued until the number of hidden neurons reached 3800, the upper limit. Thus, the three-layer RBF with 4 input neurons, 3800 hidden neurons and one output neuron were formed. As for BRN, the trial and error method was employed to determine the optimum number of hidden neurons, which led to 16. Hence, the best BRN topology (4 × 16 × 1) was finalized, with the parameters (w_1, w_2, b_1, b_2) presented in Table 5.

In this study, after the performances of both ANN models were compared, the better one was adopted for further predictions. The cross plots of predictions by both models versus the corresponding experimental values during the co-combustion process of TP73 at 20 °C·min^{-1} under the 30% O_2/70% CO_2 atmosphere were shown in Fig. 5. A tighter cloud of points fell along the 45° line showed that BRN had a more reliable prediction than did RBF. As shown in Table 6, the three performance indices (RMSE, MAE, and R^2) based on both models were compared for the co-combustion of TP73 under the different O_2/CO_2 atmospheres at 20 °C·min^{-1}. The RMSE and MAE values of BRN were lower than those of RBF, while the R^2 values showed the opposite. Fig. 6(a) illustrates the predicted TGA curves of BRN coincided with the experimental ones under the different O_2/CO_2 atmospheres. BRN provided a more robust prediction than did RBF in predicting the co-combustion properties. The predicted TGA curves based on BRN provided more groups of the O_2/CO_2 co-combustion atmospheres for TP73 (Fig. 6(b)), a similar trend with the increased O_2 concentration as discussed above.

3.4. Kinetic analysis

To evaluate the effect of the co-combustion atmosphere on the kinetics, the FWO and KAS methods were adopted to understand the oxy-fuel co-combustion process at the heating rates of 10, 20, and 30 °C·min^{-1}. The activation energy E_a values and the corresponding R^2 values from the FWO and KAS methods were summarized in Table 7 for a series of conversions ($0.2 \le \alpha \le 0.8$) for TP73 under the different atmospheres. Each deviation value of E_a obtained from the FWO and KAS methods was within 5%, reflecting their similar trends. Our results had high R^2 values in the range of 0.9514–1 (Table 7).

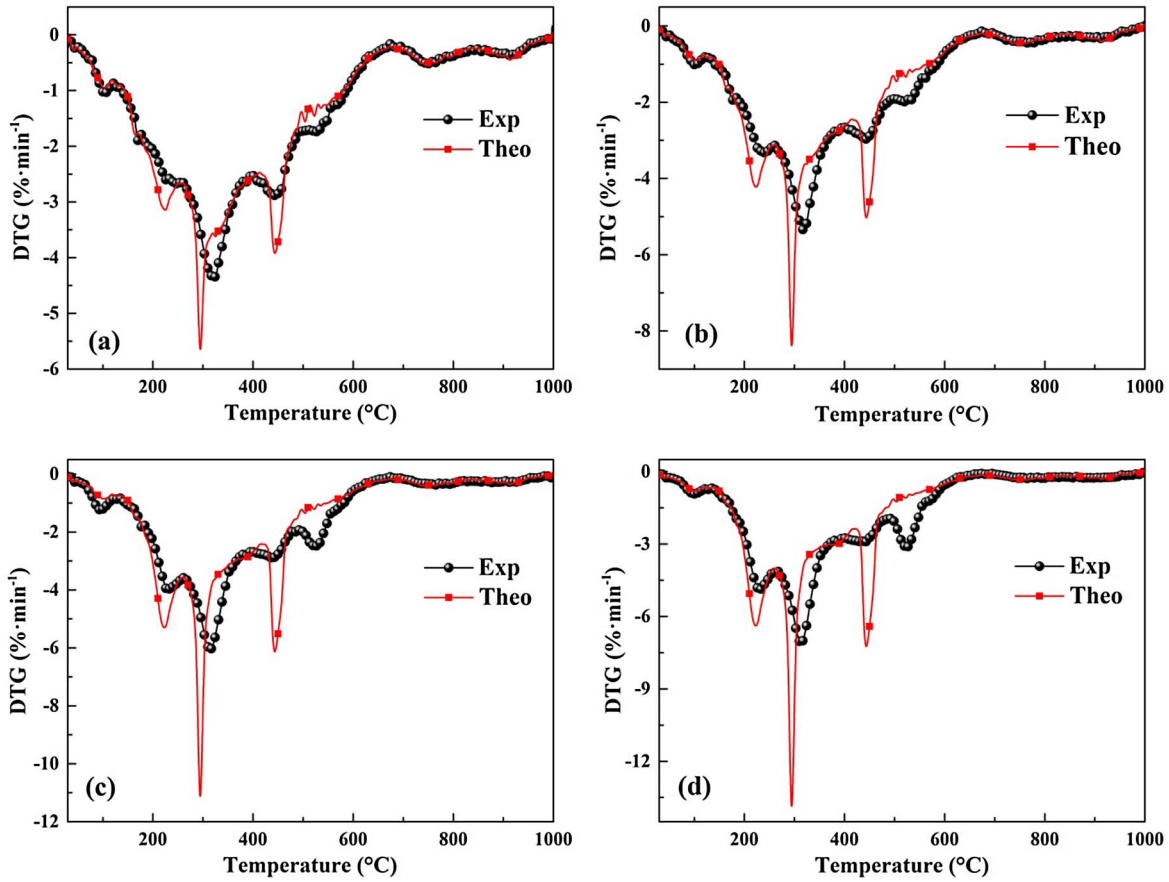

Fig. 3. The experimental and theoretical DTG curves for (a) TP91, (b) TP82, (c) TP73, and (d) TP64 at 20 °C·min^{-1} under the 30% O_2/70% CO_2 atmosphere.

In the co-combustion process of TP73, the conversion degree range of 0.2–0.6 and beyond 0.6 represented the oxidative pyrolysis of volatiles and char combustion, respectively [50]. E_a varied with the O_2/CO_2 atmospheres, showing an initial increasing trend in the conversion range of 0.2–0.5 and a subsequent decreasing trend. In particular, the significant difference among E_a values under the O_2/CO_2 atmospheres occurred in the conversion range of 0.4–0.6, which was related mainly to the maximum mass loss peak during the co-combustion process. Taking the FWO method as an example (Table 7), the average E_a values of these atmospheres were in the following order: 30% O_2/70% CO_2 (155.4 kJ·mol^{-1}) < air (160.5 kJ·mol^{-1}) < 50% O_2/50% CO_2 (167.7 kJ·mol^{-1}) < 20% O_2/80% CO_2 (177.8 kJ·mol^{-1}) < 70% O_2/30% CO_2 (205.4 kJ·mol^{-1}) < O_2 (205.8 kJ·mol^{-1}). Under the O_2/CO_2 atmosphere, E_a did not increase monotonically with the increased O_2 concentration. This finding was in good agreement with previous studies reported by Huang et al. [31]. The activation energy was affected by the change in the activated molecules concentration, diffusion and organic impurities during the co-combustion process [41]. When the O_2 concentration increased from 20% to 30%, the average E_a decreased. It was attributed to the enhanced diffusion in this stage as the O_2 concentration increased. In this stage, the higher the O_2 concentration was, the easier the proceeding of reaction was. However, the increased O_2 concentration did not always lower the activation energy and impel the proceeding of reaction. When the O_2 concentration increased from 30%

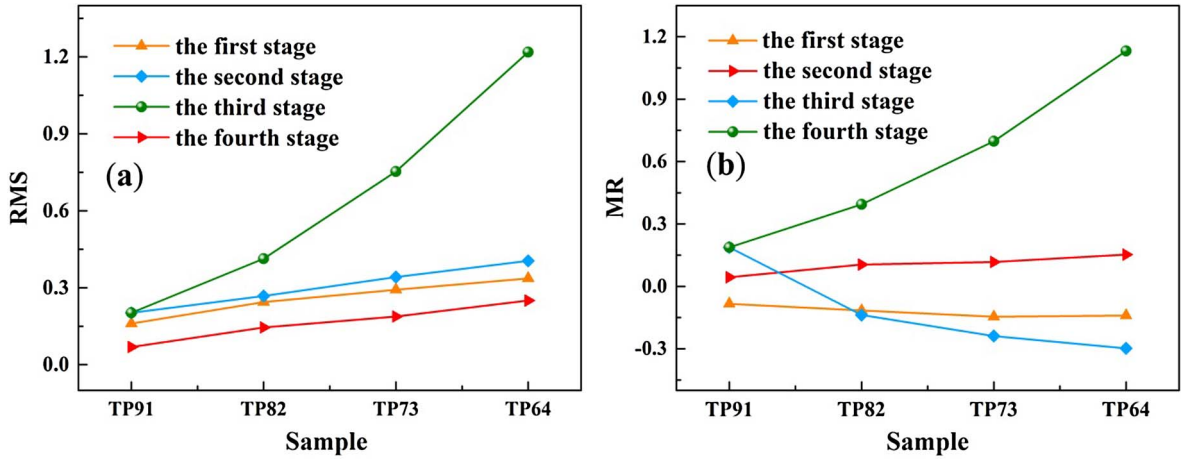

Fig. 4. The interaction indices of (a) RMS and (b) MR at 20 °C·min^{-1} under the 30% O_2/70% CO_2 atmosphere.

Table 5
Weights and biases of the best BRN topology (4 × 16 × 1).

w_1				b_1	w_2	b_2
5.4633	−11.3760	0.0706	8.2626	−7.8266	−2.1891	−9.6542
−4.0699	−3.5824	−8.6011	−4.1898	10.4975	−0.0504	
−1.5114	−6.5060	0.0325	4.6018	−4.3953	5.1212	
−4.9149	−0.1269	−0.0974	−0.1190	−0.1392	0.2799	
−0.5510	−0.4063	−0.0469	−8.9347	−3.1932	7.0265	
−0.5417	−0.5820	−0.7024	−7.6787	−3.1617	−8.3479	
0.5619	0.6141	0.7500	2.4398	1.0931	−7.1838	
−1.1783	2.8944	0.0455	−0.1017	0.2377	3.7535	
−9.8309	−2.8539	−0.1682	0.6489	−2.8560	−0.1632	
0.5818	−0.9959	−0.0262	2.1794	0.4345	5.8329	
5.1881	0.8584	0.0989	0.0594	1.8939	−0.5710	
1.4002	0.3363	−0.0193	−0.0059	1.2167	−13.6087	
0.4883	−3.3664	0.0659	3.8957	−4.3977	−8.7909	
−0.6462	−1.8458	−2.6837	−0.3361	0.9305	0.0575	
−4.2955	−8.9969	−0.0595	5.9071	−6.9313	−3.2779	
0.8914	0.3823	−0.0241	−0.0008	0.6953	18.3265	

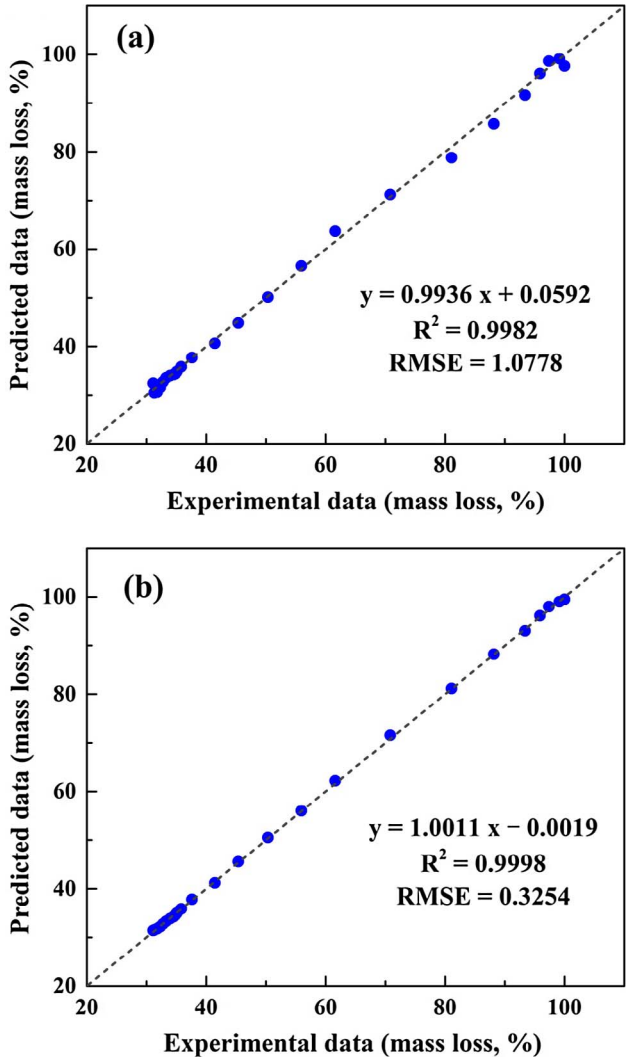

Fig. 5. Comparison of (a) RBF- and (b) BRN-predicted data versus experimental data during the co-combustion process of TP73 at 20 °C·min^{-1} under the 30% O_2/70% CO_2 atmosphere.

to 70%, heat release from semi-coke oxidization increased, and thus, the surface temperature of semi-coke increased [41]. Meanwhile, the semi-coke structure expanded the grain size and the ash content increased with the increased final temperature [37]. Therefore, the

Table 6
Comparison of performance indices for RBF and BRN for the co-combustion process of TP73 at 20 °C·min^{-1} under the O_2/CO_2 atmosphere.

Atmosphere	RMSE		MAE		R^2	
	RBF	BRN	RBFN	BRN	RBF	BRN
20% O_2/80% CO_2	0.8989	0.4957	2.2467	1.2996	0.9988	0.9996
30% O_2/70% CO_2	0.8506	0.3277	2.4981	0.9200	0.9989	0.9998
50% O_2/50% CO_2	1.0778	0.3254	2.5779	1.2946	0.9982	0.9998
70% O_2/30% CO_2	1.1066	0.3585	2.5137	1.1615	0.9981	0.9998
O_2	1.3329	0.4082	3.6004	1.5812	0.9973	0.9997

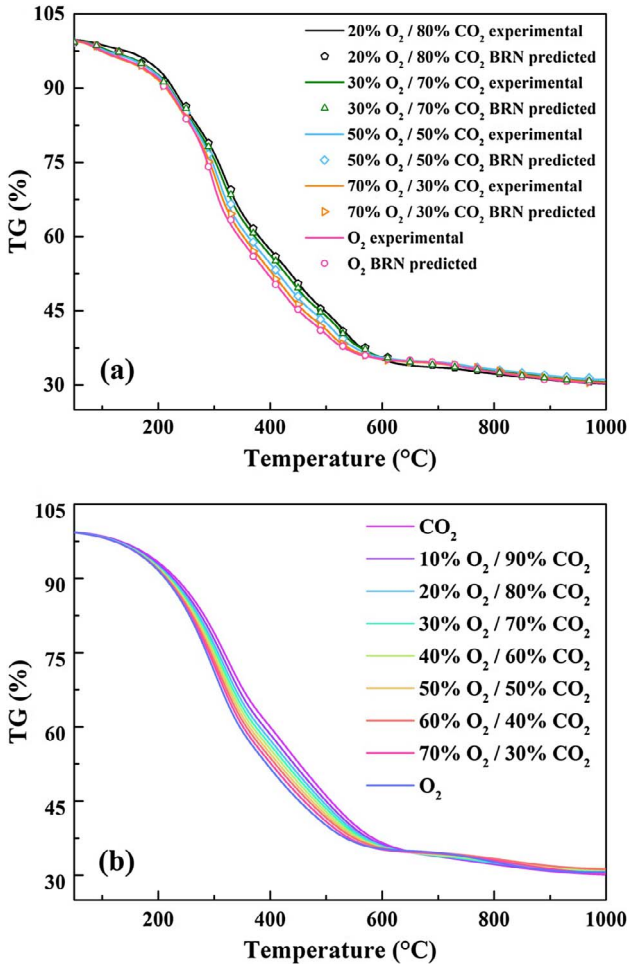

Fig. 6. TGA curves of TP73 co-combustion at 20 °C·min^{-1} under the O_2/CO_2 atmospheres: (a) comparison of BRN-predicted data versus experimental data; (b) BRN-predicted data.

average E_a increased with increased O_2 concentration in this stage. As the O_2 concentration increased from 70% to 100%, the change in average E_a was minor. This was due to very little char remained at high oxygen concentrations and combustion was not a major event [37]. The lower the activation energy was, the easier the reaction was. Hence, merely increasing the oxygen concentration was not necessarily favorable for the co-combustion of TP73.

4. Conclusions

(1) The co-combustion performance under the O_2/CO_2 atmosphere was significantly improved with the increased O_2 concentration. As the O_2 concentration increased, T_i and T_m decreased, whereas R_p, CCI and R_w increased. The 30% O_2/70% CO_2 atmosphere achieved a

Table 7
Kinetic parameter estimates from FWO and KAS for TP73 under the different atmospheres.

Atmospheres	α	FWO method			KAS method		
		Fitting equation	E_a(kJ·mol^{-1})	R^2	Fitting equation	E_a(kJ·mol^{-1})	R^2
Air	0.2	y = −9040.7x + 18.915	164.6	1.0000	y = −19795x + 29.08	164.6	1.0000
	0.3	y = −10280x + 19.787	187.1	0.9999	y = −22562x + 30.926	187.6	0.9999
	0.4	y = −9875.8x + 18.107	179.8	0.9985	y = −21569x + 26.949	179.3	0.9983
	0.5	y = −9576.1x + 16.84	174.3	0.9965	y = −20822x + 23.936	173.1	0.9960
	0.6	y = −8042.7x + 13.46	146.4	0.9985	y = −17203x + 16.013	143.0	0.9982
	0.7	y = −7295.4x + 11.522	132.8	0.9997	y = −15380x + 11.401	127.9	0.9997
	0.8	y = −7591.4x + 11.122	138.2	1.0000	y = −15945x + 10.323	132.6	1.0000
	Average		160.5			158.3	
20% O_2/80% CO_2	0.2	y = −9972.2x + 20.467	181.5	0.9827	y = −21926x + 32.628	182.3	0.9811
	0.3	y = −10735x + 20.421	195.4	0.9901	y = −23600x + 32.369	196.2	0.9892
	0.4	y = −10691x + 19.39	194.6	0.9959	y = −23441x + 29.893	194.9	0.9955
	0.5	y = −10976x + 18.993	199.8	0.9993	y = −24039x + 28.88	199.9	0.9992
	0.6	y = −9088.7x + 14.923	165.5	0.9990	y = −19599x + 19.364	162.9	0.9989
	0.7	y = −8108.9x + 12.574	147.6	0.9995	y = −17241x + 13.807	143.3	0.9994
	0.8	y = −8811.2x + 12.62	160.4	0.9990	y = −18740x + 13.756	155.8	0.9987
	Average		177.8			176.5	
30% O_2/70% CO_2	0.2	y = −8029.1x + 16.872	146.2	0.9967	y = −17462x + 24.37	145.2	0.9964
	0.3	y = −9136.1x + 17.733	166.3	0.9968	y = −19930x + 26.199	165.7	0.9964
	0.4	y = −9610.8x + 17.736	175.0	0.9901	y = −20966x + 26.107	174.3	0.9891
	0.5	y = −9834.2x + 17.377	179.0	0.9828	y = −21428x + 25.191	178.2	0.9809
	0.6	y = −8281.8x + 13.93	150.8	0.9872	y = −17767x + 17.117	147.7	0.9853
	0.7	y = −7483.6x + 11.885	136.2	0.9939	y = −15829x + 12.259	131.6	0.9929
	0.8	y = −7417.9x + 10.998	134.6	0.9928	y = −15564x + 10.06	129.4	0.9915
	Average		155.4			153.2	
50% O_2/50% CO_2	0.2	y = −8557.1x + 17.943	155.8	0.9979	y = −18679x + 26.837	155.3	0.9976
	0.3	y = −9668x + 18.808	176.0	0.9995	y = −21161x + 28.687	175.9	0.9994
	0.4	y = −11143x + 20.58	202.9	0.9995	y = −24506x + 32.677	203.7	0.9995
	0.5	y = −11736x + 20.799	213.6	0.9997	y = −25825x + 33.1	214.7	0.9997
	0.6	y = −8623.9x + 14.705	157.0	0.9994	y = −18577x + 18.935	154.4	0.9993
	0.7	y = −7474x + 12.076	136.1	0.9989	y = −15830x + 12.733	131.6	0.9986
	0.8	y = −7298.9x + 11.043	132.9	0.9983	y = −15317x + 10.201	127.3	0.9979
	Average		167.7			166.2	
70% O_2/30% CO_2	0.2	y = −12036x + 24.839	219.1	0.9708	y = −26693x + 42.722	221.9	0.9686
	0.3	y = −12290x + 23.68	223.7	0.9855	y = −27203x + 39.913	226.2	0.9843
	0.4	y = −12960x + 23.857	235.9	0.9964	y = −28695x + 40.231	238.6	0.9961
	0.5	y = −14700x + 25.903	267.6	0.9958	y = −32655x + 44.862	271.5	0.9954
	0.6	y = −10591x + 17.911	192.8	0.9863	y = −23115x + 26.332	192.2	0.9847
	0.7	y = −8492.7x + 13.65	154.6	0.9795	y = −18184x + 16.369	151.2	0.9762
	0.8	y = −7915.4x + 11.958	144.1	0.9589	y = −16744x + 12.32	139.2	0.9514
	Average		205.4			205.8	
O_2	0.2	y = −8833.3x + 18.508	160.8	0.9878	y = −19316x + 28.139	160.6	0.9865
	0.3	y = −10612x + 20.697	193.2	0.9981	y = −23345x + 33.053	194.1	0.9979
	0.4	y = −14488x + 26.783	263.7	0.9999	y = −32227x + 46.989	267.9	0.9999
	0.5	y = −18098x + 32.005	329.5	1.0000	y = −40497x + 58.941	336.7	1.0000
	0.6	y = −10354x + 17.763	188.5	0.9995	y = −22587x + 26.02	187.8	0.9994
	0.7	y = −8498.5x + 13.846	154.7	0.9999	y = −18221x + 16.856	151.5	0.9999
	0.8	y = −8235x + 12.566	149.9	0.9976	y = −17508x + 13.756	140.7	0.9971
	Average		205.8			205.6	

combustion performance analogous to air.

(2) The blending of PP with TDS significantly improved the oxy-fuel co-combustion performance. The main co-combustion process was divided into the four stages based on PCA. The interaction of the blends occurred mainly between 490 and 600 °C where the mono-combustion of TDS residue was improved. The fierce interactions existed in the fourth stage based on RMS, while the accelerative effect existed in the fourth stage and the slight inhibition existed in the second and third stages based on MR.

(3) RBF and BRN were developed to predict TGA data under the different O_2/CO_2 atmospheres. The best three-layer topology was obtained to be $4 \times 3800 \times 1$ and $4 \times 16 \times 1$ for RBF and BRN, respectively. BRN model had a more reliable and robust prediction than did RBF. BRN was applied to predict the co-combustion process under the O_2/CO_2 atmospheres.

(4) The oxy-fuel combustion kinetic analysis of TP73 was performed using the FWO and KAS methods. The lowest average E_a value (155.4 kJ·mol^{-1} by FWO and 153.2 kJ·mol^{-1}by KAS) occurred under the 30% O_2/70% CO_2 atmosphere.

(5) Our quantification and characterization results help to adopt appropriate co-combustion atmospheres and blending ratios to obtain accurate co-combustion kinetics when TDS is used in industry. The introduction and application of BRN paves the way for the modeling of TDS-related thermal process, even the determination of optimum operating conditions.

Acknowledgements

This work was supported by the Scientific and Technological Planning Project of Guangzhou, China (No. 2016201604030058; No. 201704030109), the Science and Technology Planning Project of Guangdong Province, China (No. 2015B020235013; 2017A050501036; 2017A040403045; 2017A040403044), and the Guangdong Special Support Program for Training High Level Talents (No. 2014TQ01Z248).

References

[1] Lin M, Ning X, An T, Zhang J, Chen C, Ke Y, et al. Degradation of polycyclic aromatic hydrocarbons (PAHs) in textile dyeing sludge with ultrasound and Fenton processes: effect of system parameters and synergistic effect study. J Hazard Mater 2016;307:7–16.

[2] Holkar CR, Jadhav AJ, Pinjari DV, Mahamuni NM, Pandit AB. A critical review on textile wastewater treatments: possible approaches. J Environ Manage 2016;182:351–66.

[3] Zhang H, Gao Z, Ao W, Li J, Liu G, Fu J, et al. Microwave pyrolysis of textile dyeing sludge in a continuously operated auger reactor: char characterization and analysis. J Hazard Mater 2017;334:112–20.

[4] Liang J, Ning X, Lai X, Zou H, Sun J, Lu X, et al. Influence mechanisms of textile-dyeing sludge characteristics on degradation of anilines by integrated ultrasound-permanganate treatment. J Clean Prod 2017;151:172–8.

[5] Hu Z, Ma X, Chen Y, Liao Y, Wu J, Yu Z, et al. Co-combustion of coal with printing and dyeing sludge: Numerical simulation of the process and related NO_x emissions. Fuel 2015;139:606–13.

[6] Zhuo Z, Liu J, Sun S, Sun J, Kuo J, Chang K, et al. Thermogravimetric characteristics of textile dyeing sludge, coal and their blend in N_2/O_2 and CO_2/O_2 atmospheres. Appl Therm Eng 2017;111:87–94.

[7] Peng X, Ma X, Xu Z. Thermogravimetric analysis of co-combustion between microalgae and textile dyeing sludge. Bioresour Technol 2015;180:288–95.

[8] Lou R, Wu S, Lv G, Yang Q. Energy and resource utilization of deinking sludge pyrolysis. Appl Energy 2012;90:46–50.

[9] Xiao H, Ma X, Lai Z. Isoconversional kinetic analysis of co-combustion of sewage sludge with straw and coal. Appl Energy 2009;86:1741–5.

[10] Jiang L, Yuan X, Xiao Z, Liang J, Li H, Cao L, et al. A comparative study of biomass pellet and biomass-sludge mixed pellet: energy input and pellet properties. Energy Convers Manage 2016;126:509–15.

[11] Cai Z, Ma X, Fang S, Yu Z, Lin Y. Thermogravimetric analysis of the co-combustion of eucalyptus residues and paper mill sludge. Appl Therm Eng 2016;106:938–43.

[12] Shuang-quan Z, Xiao-ming Y, Zhi-yuan Y, Ting-ting P, Ming-jian D, Tian-yu S. Study of the co-pyrolysis behavior of sewage-sludge/rice-straw and the kinetics. Proc Earth Planet Sci 2009;1:661–6.

[13] Chen C, Ma X, Liu K. Thermogravimetric analysis of microalgae combustion under different oxygen supply concentrations. Appl Energy 2011;88:3189–96.

[14] Choi IS, Lee YG, Khanal SK, Park BJ, Bae HJ. A low-energy, cost-effective approach to fruit and citrus peel waste processing for bioethanol production. Appl Energy 2015;140:65–74.

[15] Huang R, Cao M, Guo H, Qi W, Su R, He Z. Enhanced ethanol production from pomelo peel waste by integrated hydrothermal treatment, multienzyme formulation, and fed-batch operation. J Agr Food Chem 2014;62:4643–51.

[16] Bu C, Liu D, Chen X, Pallarès D, Gómez-Barea A. Ignition behavior of single coal particle in a fluidized bed under O_2/CO_2 and O_2/N_2 atmospheres: A combination of visual image and particle temperature. Appl Energy 2014;115:301–8.

[17] Selosse S, Ricci O. Carbon capture and storage: Lessons from a storage potential and localization analysis. Appl Energy 2017;188:32–44.

[18] Theo WL, Lim JS, Hashim H, Mustaffa AA, Ho WS. Review of pre-combustion capture and ionic liquid in carbon capture and storage. Appl Energy 2016;183:1633–63.

[19] Niu S, Lu C, Han K, Zhao J. Thermogravimetric analysis of combustion characteristics and kinetic parameters of pulverized coals in oxy-fuel atmosphere. J Therm Anal Calorim 2009;98:267.

[20] Niu S, Han K, Lu C. Characteristic of coal combustion in oxygen/carbon dioxide atmosphere and nitric oxide release during this process. Energy Convers Manage 2011;52:532–7.

[21] Gil MV, Riaza J, Álvarez L, Pevida C, Pis JJ, Rubiera F. Oxy-fuel combustion kinetics and morphology of coal chars obtained in N_2 and CO_2 atmospheres in an entrained flow reactor. Appl Energy 2012;91:67–74.

[22] Lai Z, Ma X, Tang Y, Lin H. A study on municipal solid waste (MSW) combustion in N_2/O_2 and CO_2/O_2 atmosphere from the perspective of TGA. Energy 2011;36:819–24.

[23] Li Q, Meng Q, Cai J, Yoshino H, Mochida A. Predicting hourly cooling load in the building: a comparison of support vector machine and different artificial neural networks. Energy Convers Manage 2009;50:90–6.

[24] Kim Y, Jang H, Kim J, Lee J. Prediction of storage efficiency on CO_2 sequestration in deep saline aquifers using artificial neural network. Appl Energy 2017;185, Part 1:916–28.

[25] Fazilat H, Akhlaghi S, Shiri ME, Sharif A. Predicting thermal degradation kinetics of nylon6/feather keratin blends using artificial intelligence techniques. Polymer 2012;53:2255–64.

[26] Buyukada M. Co-combustion of peanut hull and coal blends: artificial neural networks modeling, particle swarm optimization and Monte Carlo simulation. Bioresour Technol 2016;216:280–6.

[27] Chen J, Liu J, He Y, Huang L, Sun S, Sun J, et al. Investigation of co-combustion characteristics of sewage sludge and coffee grounds mixtures using thermogravimetric analysis coupled to artificial neural networks modeling. Bioresour Technol 2017;225:234–45.

[28] Chen S, Lior N, Xiang W. Coal gasification integration with solid oxide fuel cell and chemical looping combustion for high-efficiency power generation with inherent CO_2 capture. Appl Energy 2015;146:298–312.

[29] Xiang Y, Zhou J, Lin B, Xue X, Tian X, Luo Z. Exergetic evaluation of renewable light olefins production from biomass via synthetic methanol. Appl Energy 2015;157:499–507.

[30] Chen J, Mu L, Cai J, Yin H, Song X, Li A. Thermal characteristics and kinetics of refining and chemicals wastewater, lignite and their blends during combustion. Energy Convers Manage 2015;100:201–11.

[31] Huang L, Liu J, He Y, Sun S, Chen J, Sun J, et al. Thermodynamics and kinetics parameters of co-combustion between sewage sludge and water hyacinth in CO_2/O_2 atmosphere as biomass to solid biofuel. Bioresour Technol 2016;218:631–42.

[32] Yang Y, Lu X, Wang Q. Investigation on the co-combustion of low calorific oil shale and its semi-coke by using thermogravimetric analysis. Energy Convers Manage 2017;136:99–107.

[33] Wang Q, Zhao W, Liu H, Jia C, Li S. Interactions and kinetic analysis of oil shale semi-coke with cornstalk during co-combustion. Appl Energy 2011;88:2080–7.

[34] Mani-Varnosfaderani A, Kanginejad A, Gilany K, Valadkhani A. Estimating complicated baselines in analytical signals using the iterative training of Bayesian regularized artificial neural networks. Anal Chim Acta 2016;940:56–64.

[35] Wang CA, Zhang X, Liu Y, Che D. Pyrolysis and combustion characteristics of coals in oxyfuel combustion. Appl Energy 2012;97:264–73.

[36] Meng F, Yu J, Tahmasebi A, Han Y. Pyrolysis and combustion behavior of coal gangue in O_2/CO_2 and O_2/N_2 mixtures using thermogravimetric analysis and a drop tube furnace. Energy Fuels 2013;27:2923–32.

[37] López-González D, Parascanu MM, Fernandez-Lopez M, Puig-Gamero M, Soreanu G, Avalos-Ramírez A, et al. Effect of different concentrations of O_2 under inert and CO_2 atmospheres on the swine manure combustion process. Fuel 2017;195:23–32.

[38] Shaddix CR, Molina A. Particle imaging of ignition and devolatilization of pulverized coal during oxy-fuel combustion. P Combust Inst 2009;32:2091–8.

[39] Riaza J, Gil MV, Álvarez L, Pevida C, Pis JJ, Rubiera F. Oxy-fuel combustion of coal and biomass blends. Energy 2012;41:429–35.

[40] Li X, Rathnam RK, Yu J, Wang Q, Wall T, Meesri C. Pyrolysis and combustion characteristics of an Indonesian low-rank coal under O_2/N_2 and O_2/CO_2 conditions. Energy Fuels 2009;24:160–4.

[41] Chen C, Lu Z, Ma X, Long J, Peng Y, Hu L, et al. Oxy-fuel combustion characteristics and kinetics of microalgae Chlorella vulgaris by thermogravimetric analysis. Bioresour Technol 2013;144:563–71.

[42] Zhang L, Binner E, Qiao Y, Li C. In situ diagnostics of Victorian brown coal combustion in O_2/N_2 and O_2/CO_2 mixtures in drop-tube furnace. Fuel 2010;89:2703–12.

[43] Li Q, Zhao C, Chen X, Wu W, Li Y. Comparison of pulverized coal combustion in air and in O_2/CO_2 mixtures by thermo-gravimetric analysis. J Anal Appl Pyrol 2009;85:521–8.

[44] Ma J, Wang Z, Zhu C, Xu Y, Wu Z. Electrogenesis reduces the combustion efficiency of sewage sludge. Appl Energy 2014;114:283–9.

[45] Mu L, Chen J, Yao P, Zhou D, Zhao L, Yin H. Evaluation of co-pyrolysis petrochemical wastewater sludge with lignite in a thermogravimetric analyzer and a packed-bed reactor: pyrolysis characteristics, kinetics, and products analysis. Bioresour Technol 2016;221:147–56.

[46] Zhou C, Liu G, Wang X, Qi C. Co-combustion of bituminous coal and biomass fuel blends: thermochemical characterization, potential utilization and environmental advantage. Bioresour Technol 2016;218:418–27.

[47] Lin Y, Ma X, Yu Z, Cao Y. Investigation on thermochemical behavior of co-pyrolysis between oil-palm solid wastes and paper sludge. Bioresour Technol 2014;166:444–50.

[48] Zhang Y, Zhang Z, Zhu M, Cheng F, Zhang D. Interactions of coal gangue and pine sawdust during combustion of their blends studied using differential thermogravimetric analysis. Bioresour Technol 2016;214:396–403.

[49] Yanfen L, Xiaoqian M. Thermogravimetric analysis of the co-combustion of coal and paper mill sludge. Appl Energy 2010;87:3526–32.

[50] Idris SS, Rahman NA, Ismail K. Combustion characteristics of Malaysian oil palm biomass, sub-bituminous coal and their respective blends via thermogravimetric analysis (TGA). Bioresour Technol 2012;123:581–91.